Journal of Ship Research, Vol. 64, No. 4, December 2020, pp. 346–356
http://dx.doi.org/10.5957/JOSR.09180081

Study of a Container Ship with Breaking Waves at High Froude Number Using URANS and DDES Methods

Jianhua Wang, Zhen Ren, and **Decheng Wan**

State Key Laboratory of Ocean Engineering, School of Naval Architecture, Ocean and Civil Engineering, Shanghai Jiao Tong University, Collaborative Innovation Center for Advanced Ship and Deep-Sea Exploration, Shanghai, China

The KRISO container ship model is used for numerical simulations to investigate hydrodynamic performance under high speeds. Unsteady Reynolds-Averaged Navier-Stokes (URANS) and delayed detached eddy simulation (DDES) approaches are used to resolve the flow field around the ship model. High-resolution Volume of Fluid (VOF) technique in OpenFOAM is used to capture the free surface. The present work focuses on the wave-breaking phenomena of high-speed ships. To study the speed effects on the phenomenon of ship bow wave breaking, three different speeds, i.e., Fn = .26, .35, and .40, are investigated for a fixed ship model in calm water. Predicted resistance and wave patterns under Fn = .26 are validated with available experimental data, and a good agreement is achieved. The breaking wave phenomena can be observed from both URANS and DDES results for Froude numbers greater than .35. And the Fn = .40 case shows more violent breaking bow waves. The process of overturning and breaking of bow wave is more complex in the DDES results, and some small-scale free surface features are also captured. The predicted bow wave is compared with the experiment conducted at the China Ship Scientific Research Center. It shows that the DDES results are more accurate. Wave profiles and vorticity field at several cross sections are presented to illustrate the relationship between bow waves and vortices. It is found that the free surface vorticity dissipates quickly in the URANS simulation, which leads to the difference compared with the DDES results.

Keywords: breaking bow waves; free surface flows; DDES method; ship hydrodynamics

1. Introduction

Ship advancing in calm water is one of the most fundamental studies in ship hydrodynamics research. Although ship resistance can be well predicted, it is still challenging to accurately resolve the flow field, especially for the breaking wave phenomenon of high-speed surface ships. To gain a better understanding of the physical phenomena for high-speed ships, extensive experimental studies have been conducted worldwide to try to explain the breaking wave mechanism and provide abundant computational fluid dynamics (CFD) validation data. Dong et al. (1997) performed an experimental study using particle image velocimetry measurements and free surface visualizations around a ship model at two different speeds, i.e., Fn = .28 and Fn = .45. Wave-breaking phenomenon was observed and the breaking wave associated with vorticity was further discussed. Roth et al. (1999) applied the same approach in the experimental study for DDG-51 model 5422 at Froude number .30. Through the measurements of flow structure and turbulence within the bow wave region, it was found that negative vorticity was generated at the toe of the wave and positive vorticity appeared on the top of the wave as well as at the ship boundary. Longo and Stern (2002) performed mean velocity and wave elevation measurements for the static drift condition, which showed the presence of a bow wave-breaking–induced vortex on the windward side of the model. Olivieri et al. (2007) performed an experimental study for the high-speed surface combatant model DTMB 5415, where scars and vortices

Manuscript received by SNAME headquarters May 15, 2019; accepted October 2, 2019.

Corresponding author: Decheng Wan, dcwan@sjtu.edu.cn

induced by ship bow and shoulder waves were analyzed. In addition, wake profile and vorticity distribution were also discussed.

With the development of numerical algorithms and the boost of high-performance computing, CFD has become a powerful tool in the research of ship hydrodynamics. Wilson et al. (2006) adopted the URANS solver, CFDSHIP-IOWA, to predict the hydrodynamic performance of a high-speed surface ship (R/V *Athena I*) under different speeds (Fr = .25, .43, and .62). A single-phase level-set method was used to capture free surface, and structured overset grids were used to refine the local regions near the bow and transom waves. Good agreement was achieved for both velocity components and axial vorticity at four cross planes, which indicated that the CFD approach can accurately predict the detailed wake flow and breaking bow wave. Marrone et al. (2011, 2012) developed a 2D+t SPH model and a 3D SPH solver to analyze the breaking wave pattern of the vessel DTMB 5365, and the overturning and breaking of bow waves were captured clearly. The results were also compared with the measurements and numerical results from RANS simulations in which the level set method was applied to resolve the free surface.

Apart from the RANS and meshless approaches, many studies based on detached eddy simulations (DESs) (Spalart et al. 2006; Spalart 2009) were carried out recently in the research of ship hydrodynamics. Carrica et al. (2010) performed large-scale DES computations for the surface combatant DTMB 5512 using more than 60 million cells. The simulation results showed very significant improvements in the local flow and free surface results but minor improvements in forces and moments when compared with previous URANS computations with coarser grids. Mousaviraad et al. (2015) conducted DES computations for a high-speed planning craft (Fn = .59–1.78) using the single-phase level set solver CFDShip-Iowa V4.5 and the two-phase VOF solver CFDShip-Iowa V6.2. The results showed that the tails of the spray are not well resolved, and the author stated that a finer grid resolution is required for better prediction. Broglia and Durante (2018) used a single-phase level set method to accurately predict the complex free surface flow around a high-speed craft with a series of Froude numbers ranging from .6 to 1.2. The methodology is proved to be reliable in the accurate prediction of the wave pattern, velocity, and pressure fields.

The present work is a preliminary study for the high-speed KRISO container ship (KCS) model associated with breaking bow waves. The objective of this work was to find a practical approach to accurately predict complex free surface flows and examine whether the KCS model is appropriate for the wave-breaking study planned for the CFD Workshop 2021. In the present work, the in-house solver naoe-FOAM-SJTU (Wang et al. 2019) is used to complete all numerical simulations. URANS and delayed detached eddy simulation (DDES) computations with a high-resolution VOF technique are carried out to predict the hydrodynamic performance of the ship under three advancing speeds, i.e., Fn = .26, .35, and .40. In the following section, the numerical approach is reported in detail. Then, the geometry model, grid distribution, and test conditions are shown. Subsequently, numerical results with validation in lower speed and wave patterns, and free surface vortices in high speeds are further discussed. Finally, the conclusion of this article is drawn.

2. Numerical approach

The in-house CFD solver naoe-FOAM-SJTU (Shen et al. 2015; Cao & Wan 2017; Wang et al. 2017; Ye & Wan 2017; Wang et al. 2018), developed on the open-source platform OpenFOAM, is used for the numerical computations. Navier–Stokes equations are solved for unsteady turbulent flows, and the VOF method is used to capture free surface around complex geometry models. The governing equations are written as a mass conservation equation and a momentum conservation equation:

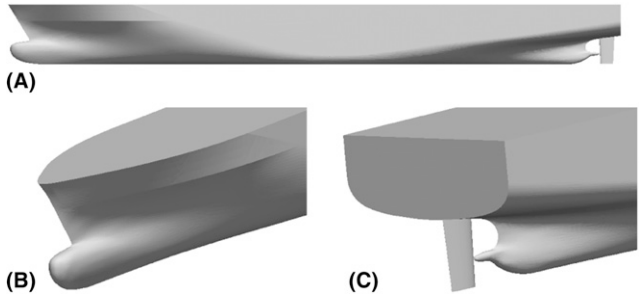

Fig. 1 KCS geometry model: (A) Profile view; (B) bow view; and (C) stern view

$$\nabla \cdot \boldsymbol{U} = 0, \tag{1}$$

$$\frac{\partial \rho \boldsymbol{U}}{\partial t} + \nabla \cdot (\rho \boldsymbol{U}\boldsymbol{U}) = -\nabla p_d - \boldsymbol{g} \cdot \boldsymbol{x} \nabla \rho + \nabla \cdot \left(\mu_{\text{eff}} \nabla \boldsymbol{U}\right) + (\nabla \boldsymbol{U}) \cdot \nabla \mu_{\text{eff}} + f_\sigma, \tag{2}$$

where $\boldsymbol{U}$ is the fluid velocity field; p_d is the dynamic pressure, obtained by subtracting the hydrostatic component from the total pressure; ρ is the mixture density of the two-phase fluid; $\mu_{eff} = \rho(\nu + \nu_t)$ is the effective dynamic viscosity, in which ν and ν_t are the kinematic viscosity and kinematic eddy viscosity, respectively, and the latter is obtained by Menter's blending turbulence model SST $k - \omega$ (Menter et al. 2003); and f_σ is a source term due to surface tension.

The two-equation SST model has been proven to be accurate and robust for ship and ocean engineering problems. For the URANS approach in OpenFOAM, the transport equation for the turbulent kinetic energy k and the specific dissipation ω is given by

$$\frac{\partial k}{\partial t} + \nabla \cdot (\boldsymbol{U}k) = \tilde{G} - \beta^* k\omega + \nabla \cdot [(\nu + \sigma_k \nu_t)\nabla k], \tag{3}$$

Table 1 Main particulars of KCS

Parameter	Full scale	Model
Scale λ	1	37.89
L_{pp} (m)	230	6.0702
L_{wl} (m)	232.5	6.1355
B (m)	32.2	.8498
Displacement (m^3)	52,030	.9565
Draft (m)	10.8	.285
Wetted surface area (with rudder)	9645	6.7182
LCG (%L aft of centroid)	1.48	1.48
GM (m)	.60	.016
I_{xx}/B	.40	.40
I_{zz}/L_{pp}	.25	.25

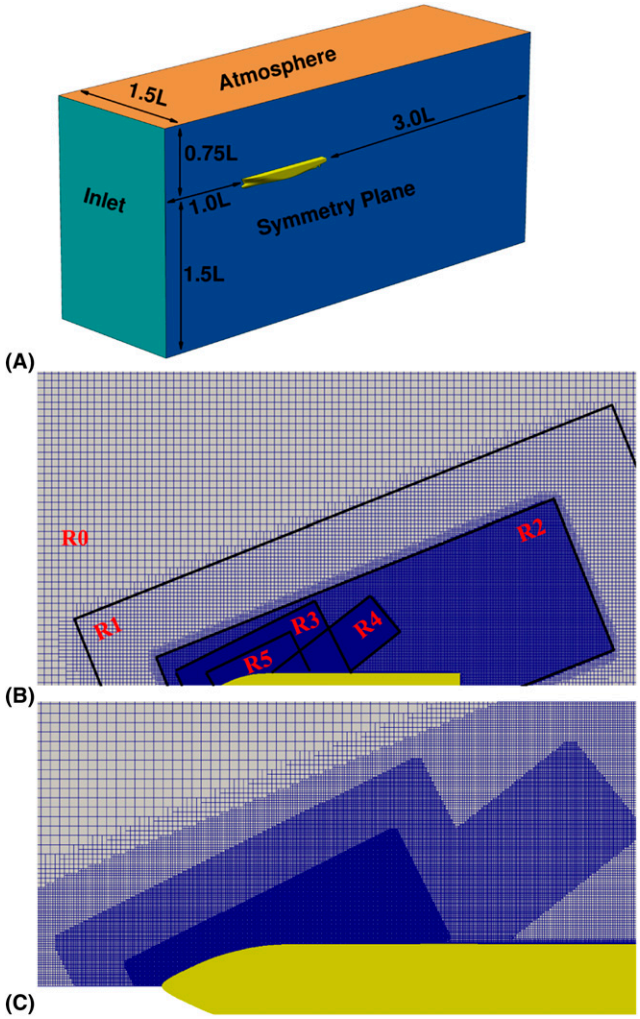

Fig. 2 (A) Computational domain and boundary conditions; (B) global view of free surface refinement; (C) low view of refinement in the bow wave region

$$\frac{\partial \omega}{\partial t} + \nabla \cdot (\boldsymbol{U}\omega) = \gamma S^2 - \beta\omega^2 + \nabla \cdot [(\nu + \sigma_\omega \nu_t)\nabla\omega] + (1 - F_1)CD_{k\omega}, \quad (4)$$

where F_1 is the blending function to achieve the blended $k-\varepsilon$ and $k-\omega$ model. Details of the SST model can be found in Menter (1994).

Table 2 Information for grid refinement

Refinement region	Location	Refine level
Hull near	R0	2
Free surface far	R1	3
Free surface near	R2	4
Bow wave far	R3	5
Shoulder wave	R4	5
Bow wave near	R5	6

Table 3 Physical quantities in experiment and simulation

Parameter	Experiment	Simulation
Water density	998.63	998.5
Kinematic viscosity	1.14×10^{-6}	1.14×10^{-6}
Surface tension	.0734	.0734
Gravity acceleration	9.81	9.81

For the DES approach, the formulation modifies the dissipation term by replacing the calculated RANS length scale l_{RANS} with a mixed length scale l_{DES}, which is defined as

$$l_{\mathrm{DES}} = \min(C_{\mathrm{DES}}\Delta, l_{\mathrm{RANS}}), \quad (5)$$

where the length scale of the SST RANS model is defined as

$$l_{\mathrm{RANS}} = \frac{\sqrt{k}}{\beta^*\omega}. \quad (6)$$

As a result, the dissipation term in the k-equation can be rewritten as

$$D^k_{\mathrm{RANS}} \equiv \beta^* k\omega = k^{3/2}/l_{\mathrm{RANS}}. \quad (7)$$

The calibrated DES constant C_{DES} is blended from two constants using Menter's blending function F_1.

$$C_{\mathrm{DES}} = (1 - F_1)C^{k-\varepsilon}_{\mathrm{DES}} + F_1 C^{k-\omega}_{\mathrm{DES}}. \quad (8)$$

Thus, the k-equation for DES becomes

$$\frac{\partial k}{\partial t} + \nabla \cdot (\boldsymbol{U}k) = \tilde{G} - \frac{k^{3/2}}{l_{\mathrm{DES}}} + \nabla \cdot [(\nu + \sigma_k \nu_t)\nabla k]. \quad (9)$$

Details about the constants and coefficients in equations can be found in Zhao and Wan (2016b). As for the DDES approach, the turbulent length scale is redefined as

$$l_{\mathrm{DDES}} = l_{\mathrm{RANS}} - f_d \max(0, l_{\mathrm{RANS}} - C_{\mathrm{DES}}\Delta), \quad (10)$$

where f_d is the empirical blending function. Details of the implementation of the DDES approach in the naoe-FOAM-SJTU solver can be found in Zhao and Wan (2016a) and Zhao et al. (2018).

In the present work, a high-resolution VOF method with a bounded compression technique (Berberović et al. 2009) is applied to sharply capture free surface, and the transport equation is expressed as

$$\frac{\partial \alpha}{\partial t} + \nabla \cdot \left[(\boldsymbol{U} - \boldsymbol{U}_{\mathrm{g}})\alpha\right] + \nabla \cdot [\boldsymbol{U}_r(1 - \alpha)\alpha] = 0, \quad (11)$$

where α is the volume of fraction; 0 and 1 represent that the cell is filled with air and water, respectively; and $0 < \alpha < 1$ stands for the

Table 4 Comparison of resistance at Fn = .26

Parameter	EFD	URANS	DDES
Sinkage ($/L_{\mathrm{pp}}$)	−2.074e-3	—	—
Trim (deg)	−.1646	—	—
C_T ($\times 10^3$)	3.835	3.662	3.654
C_F ($\times 10^3$)	—	2.768	2.643
C_P ($\times 10^3$)	—	.894	1.011

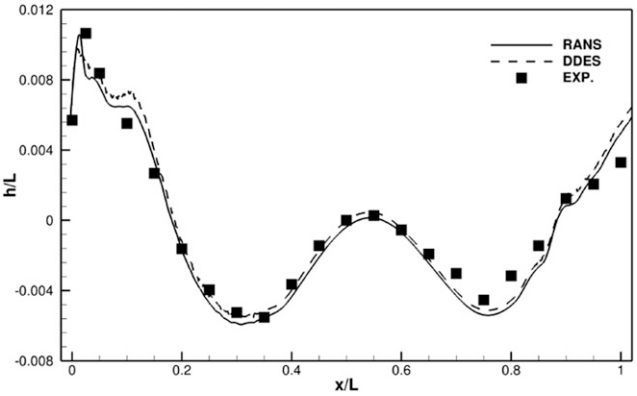

Fig. 3 Comparison of wave profile on hull surface

interface between the two-phase fluid. $\boldsymbol{U}_r$ in Equation (11) is the relative velocity used to compress the interface.

According to the literature concerning wave breaking, small-scale wave breaking is strongly influenced by surface tension. The role played by surface tension is quite different for breaking and nonbreaking waves because the surface tension pressure jump depends on the magnitude of the radius of curvature of the free surface. To accurately resolve the violent free surface flow, surface tension is taken into account in the present simulation and the surface tension term mentioned in Equation (2) is expressed as:

$$f_\sigma = \sigma\kappa\nabla\alpha, \tag{12}$$

where σ stands for the surface tension and κ is the curvature of free surface and is defined as

$$\kappa = -\nabla\cdot\boldsymbol{n} = -\frac{\sum_f \boldsymbol{S}_f\cdot\boldsymbol{n}_f}{V_i}, \tag{13}$$

where V_i represents the volume of the cell i and $\boldsymbol{S}_f$ is the normal vector of face of the cell and its magnitude equals the face area. $\sum_f \boldsymbol{S}_f$ stands for the sum of value on each face of the cell.

The computational domain is discretized by a finite volume method with fully unstructured grids. The pressure implicit splitting operator algorithm (Issa 1986) is used to decouple the pressure–velocity

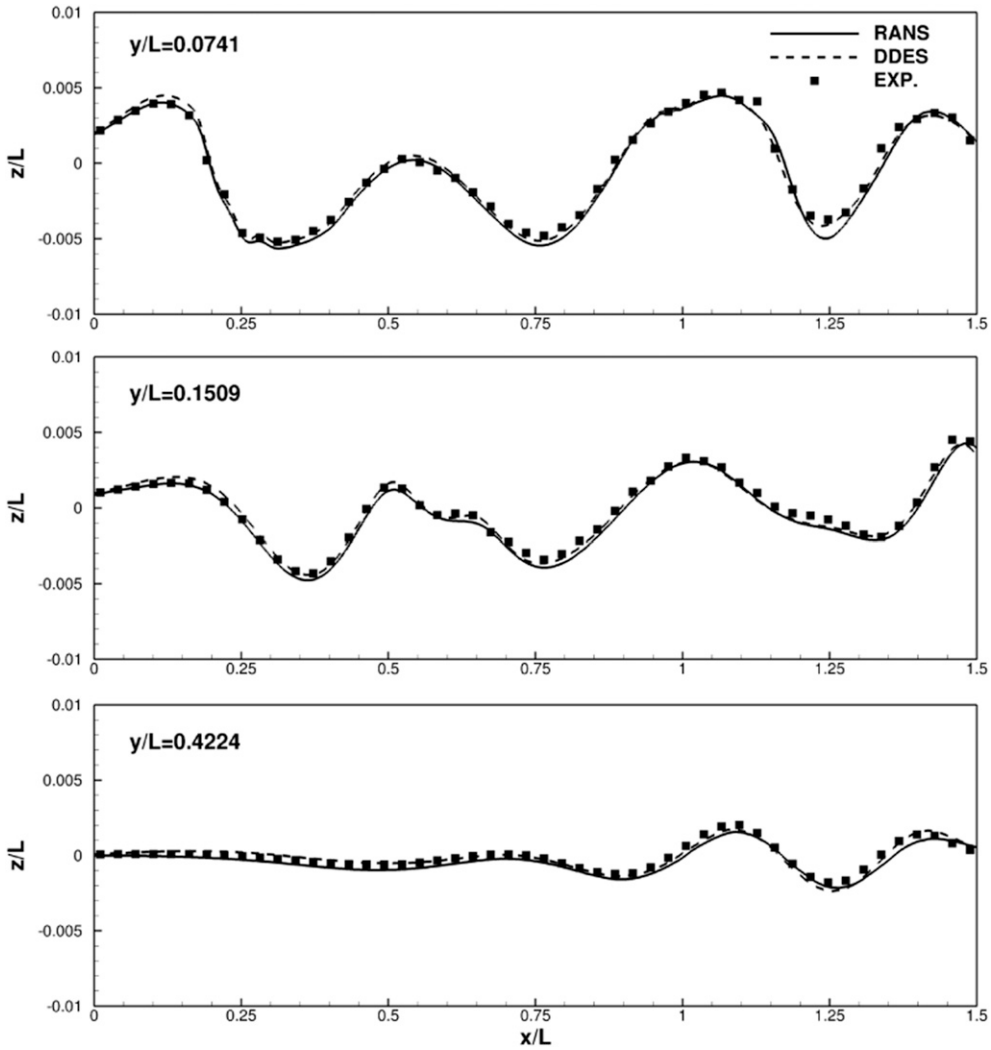

Fig. 4 Comparison of free surface cuts

equation. Several built-in numerical schemes in OpenFOAM are used to discretize and solve the partial differential equations. The convection terms are discretized by a second-order total variation diminishing (TVD) limited linear scheme, and the viscous terms are approximated by a second-order central difference scheme. A second-order backward scheme is used for temporal discretization except for the VOF advection equation, where an implicit Euler scheme is adopted. The Van Leer scheme is used for the convection term in VOF equations.

3. Computational overviews

3.1. Geometry model

The KCS model with a length of 6.0702 m is used for the present numerical computations. The ship model is fitted with a static rudder. During the simulation, the ship model is fixed with the consideration of few variables in the computation. The geometry model is shown in Fig. 1 and the main particulars are given in Table 1. This ship model is used as one of the benchmark cases in the Tokyo 2015 CFD Workshop.

3.2. Computational domain and grid distribution

The computational domain is shown in Fig. 2A. Because the ship model is fixed in the simulation, only half domain is used. The boundary conditions and dimensions are also given in the figure. The Cartesian background grid extends to $-1.0 < x/L < 4.0$; $.0 < y/L < 1.5$; and $-1.5 < z/L < .75$. The unstructured grid is generated by *Hexpress* with a total number of 7.92 million cells. The number of cells of the initial mesh is $80 \times 24 \times 36$ in the x, y, and z directions within the computational domain. The six refinement regions shown in Fig. 2B are adopted to refine the grids around the geometry and free surface, especially near the bow and shoulder waves. The locations and ranges of the refinement regions are determined according to previous studies (Wang & Wan 2017) and the Kelvin wave pattern. Mesh refinement is achieved by splitting the cells, where refine level 1 means that a cell is split into eight cells ($2 \times 2 \times 2$). For example, the refinement level of "Bow wave near" "6" means that the length of the refined cell is $(1/2)^6$ of the initial size. The size of the highest level refinement region is about 9.7e-4 nondimensioned by ship length. Figure 2C presents the local arrangement of the refinement regions. Detailed information of the refinement levels is shown in Table 2. Grid effects on the ship breaking bow waves have also been investigated in our previous study (Ren et al. 2018), and the refinement arrangement grid distribution follows the previous work. Near-wall treatment applies the wall function and the $y+$ is around 30.

3.3. Test conditions

The present simulation follows the setup of benchmark case 2.10 in the Tokyo 2015 CFD Workshop. Because wave-breaking phenomena are strongly associated with turbulence generation, the physical quantities of the fluid should be considered carefully in the numerical simulations. Table 3 summarizes the water quality and physical quantities adopted in the experiments and simulations. Three approaching speeds, namely, $U = 2.017$ m/sec, $U = 2.701$ m/sec, and $U = 3.087$ m/sec, corresponding to Froude numbers

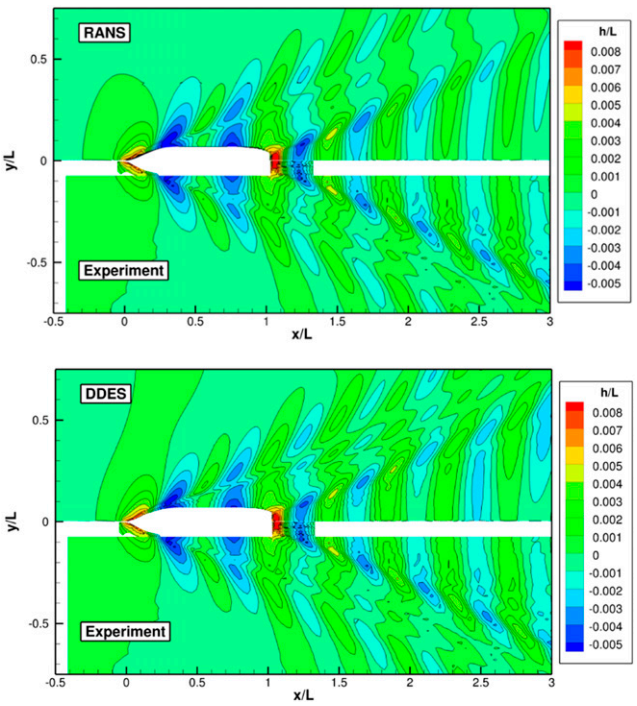

Fig. 5 Comparison of wave patterns

Fn = .26, Fn = .35, and Fn = .40, respectively, are taken into account to investigate the wave-breaking behavior.

4. Simulation results

The computations were carried out on an HPC cluster (IBM nx360M4) in Shanghai Jiao Tong University, which consists of 20 CPUs per node and 64 GB accessible memory (Intel Xeon E5-2680v2 @2.8 GHz). Three nodes with a total of 60 processors were used to calculate the flow field around the ship hull under different speeds. The time step was set to $\Delta t = .001$ second, with the mean Courant number around .02 and maximum Courant number around 4 for the whole domain, and the time to complete the computation was approximately 83 wall-clock hours, with about 50,000 time steps for wave-breaking simulations.

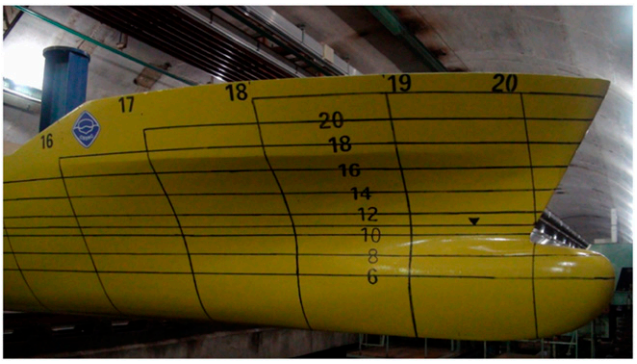

Fig. 6 KCS ship model at the CSSRC

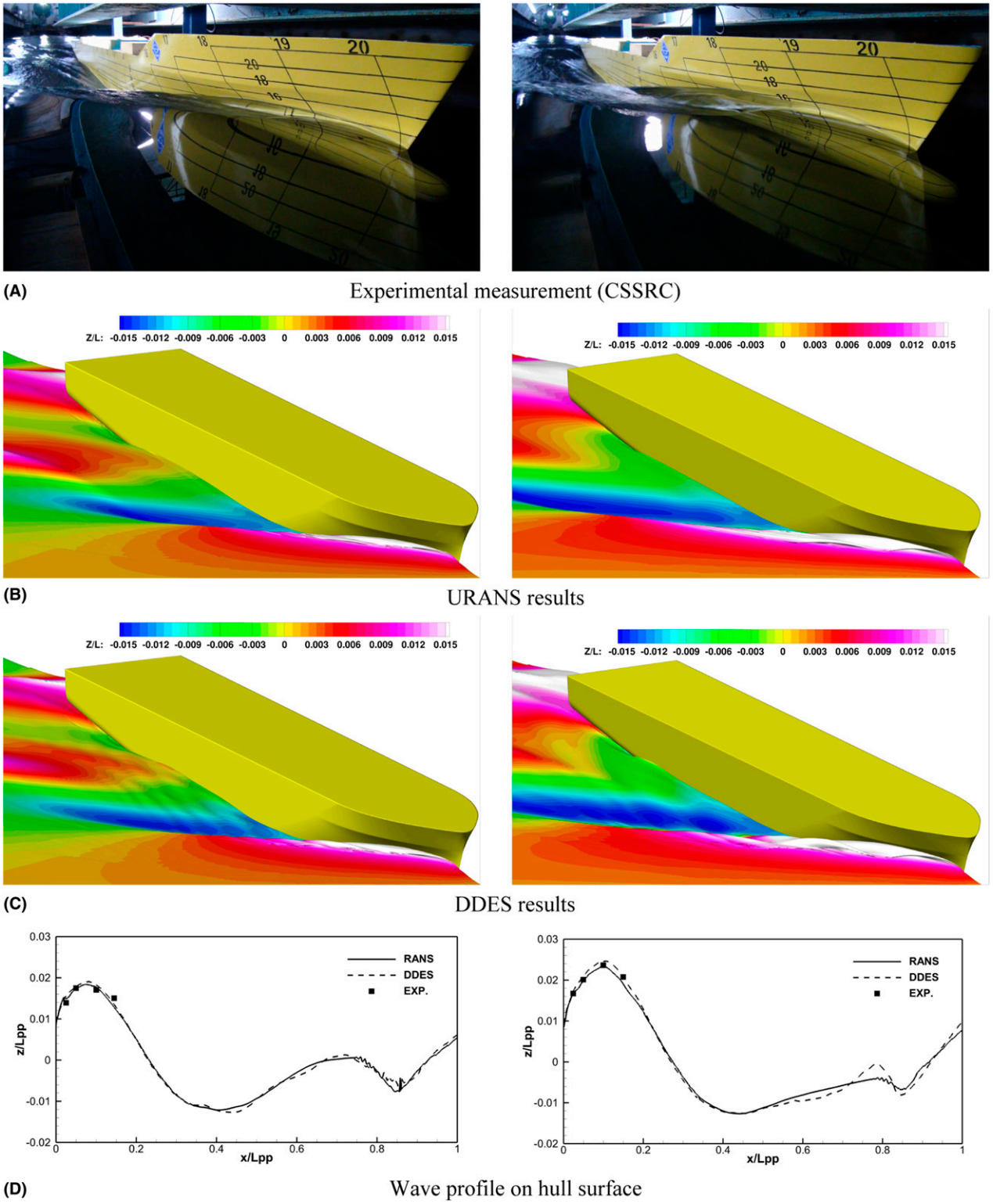

Fig. 7 Comparison of wave patterns (left column: Fn = .35, right column: Fn = .40): (A) Experimental measurement (CSSRC); (B) URANS results (C); DDES results; (D) wave profile on hull surface

4.1. Validation case with Fn = .26

The lower speed case was selected to validate the prediction accuracy as detailed experimental data including wave pattern were only available for this case. The comparison between the predicted resistance and the experiment data is shown in Table 4. The resistance coefficient was underestimated by 4.51% and 4.72% for the URANS and DDES computations, respectively. The friction resistance computed by the DDES was lower than that of the URANS approach, which also shows the same trend with the data presented by Kornev et al. (2019). The accuracy of the predicted total resistance was acceptable because the sinkage and trim were not taken into consideration in all the present simulations.

Figure 3 demonstrates wave profile comparisons between the numerical results and available measurements. It can be seen that both the URANS and DDESs can well predict the wave profile on the hull surface, where DDESs are more accurate for ship wave in the after region. To provide more validation data for the wave pattern, wave heights of three free surface cuts (y/L = .0741, .1509, and .4224) are presented in Fig. 4. It is obvious that the predicted free surface elevation agrees very well with the measurements both for the near field and far field from the ship hull from the comparison of wave height at free surface cuts. The main difference between the URANS and DDES results is the wave height at the bow wave region and stern wave region, where the DDESs perform better at the stern wave and the far-field waves. Better performance with the prediction of wave pattern for the DDES approach can also explain the good results of ship resistance shown in Table 4. The wave pattern comparison is depicted in Fig. 5. Because there was no wave breaking, the simulated results of URANS and DDESs showed little difference. The global view of the numerical results showed remarkable agreement with the measurement, which indicates that the present numerical approach is reliable. It is proved that both URANS and DDESs can give relatively good predictions for the resistance and wave pattern at lower ship speeds with no breaking waves. The accurate prediction for the validation case lays a good foundation for the next high-speed ship simulations.

4.2. High-speed case

Both URANS and DDES computations were carried out for the high-speed cases. Towing tank experiments for a smaller model ($L_{pp} = 4.3671$, as shown in Fig. 6) were conducted at the CSSRC. Photo study was the first step for the breaking bow waves in the measurements. Figure 7A presents the measured wave pattern around the KCS ship with different towing speeds. Figures 7B and C illustrate the numerical results of the free surface by the two numerical approaches at Fn = .35 and Fn = .40. Figure 7D demonstrates the comparisons between numerical results and measurements, where the experiment data of the wave profile at the hull surface were obtained by the position of wave elevation on the bow grid lines, as shown in Fig. 6. The wave ordinate was referred to the ship length. The wave patterns and the wave profile on the hull surface were compared using the time-averaged value. Only four sample data were used corresponding to the four stations at the bow area. It was found that both URANS and DDES approaches can predict well with the wave profile in the bow wave region, whereas the DDES approach is a little better than URANS through the comparison with available measurements. It can also be seen that the DDES results show more violent surface flow than the URANS results, which is also consistent with the experiment photos.

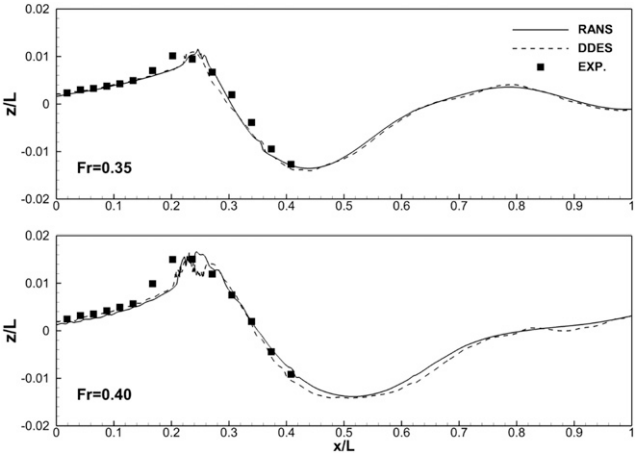

Fig. 8 Comparison of free surface cut at y/L = .1362

The breaking wave phenomena can be observed from all three approaches, although the experimental measurement showed more violent behavior toward the back of the wave. Higher speed, Fn = .40, experienced rough breaking bow waves and seemed to be more unsteady. To quantitatively compare the performance of different numerical approaches, the wave profile at a specified line ($y/L = 0.1362$) in the experiment was recorded using ultrasonic wave meter probes. Figure 8 gives the comparison of the wave profile at $y/L = 0.1362$. It can be noted that both URANS and DDES approaches can give an overall good prediction of the wave profile even at a relatively far region. The DDES approach performs a bit better than URANS, especially for the higher speed case of Fn = .40. However, both URANS and DDES results still have some discrepancies for the wave peak when compared with the measurements.

To better present the breaking bow waves, six cross sections varying from $x/L = .06$ to .16 were chosen to illustrate the bow wave elevation and the differences by URANS and DDES methods with the higher ship speed of Fn = .40. From Fig. 9, we can see that the wave height is larger in the DDESs for each section. This phenomenon is also consistent with the results of the validation case under lower ship speed. The evolution of bow waves along the longitudinal direction shows two plungers with obvious air entrainment. Significant difference can be observed after section x/L_{pp} over .1, where the crest of the wave reconnected with the free surface.

To explain the different evolutions of the breaking bow waves by URANS and DDES methods, axial vorticity distributions at cross sections are presented in Fig. 10. Five sections with x/L_{pp} equal to .05, 010, .15, .20, and .25 were used to illustrate the breaking wave phenomena. The variation of vorticity and wave field was mainly concentrated near the free surface. As shown in Fig. 10A, the initial plunger was generated because of the interaction between gravity and inertial forces when the hull blocks the inflow. The axial vorticity on free surface was slightly larger in the DDES. Both approaches can resolve the first connection between the initial plunger and the free surface with the development of an initial plunger outboard shown in Fig. 10B, where the URANS results experience earlier connection. When looking into the high curvature

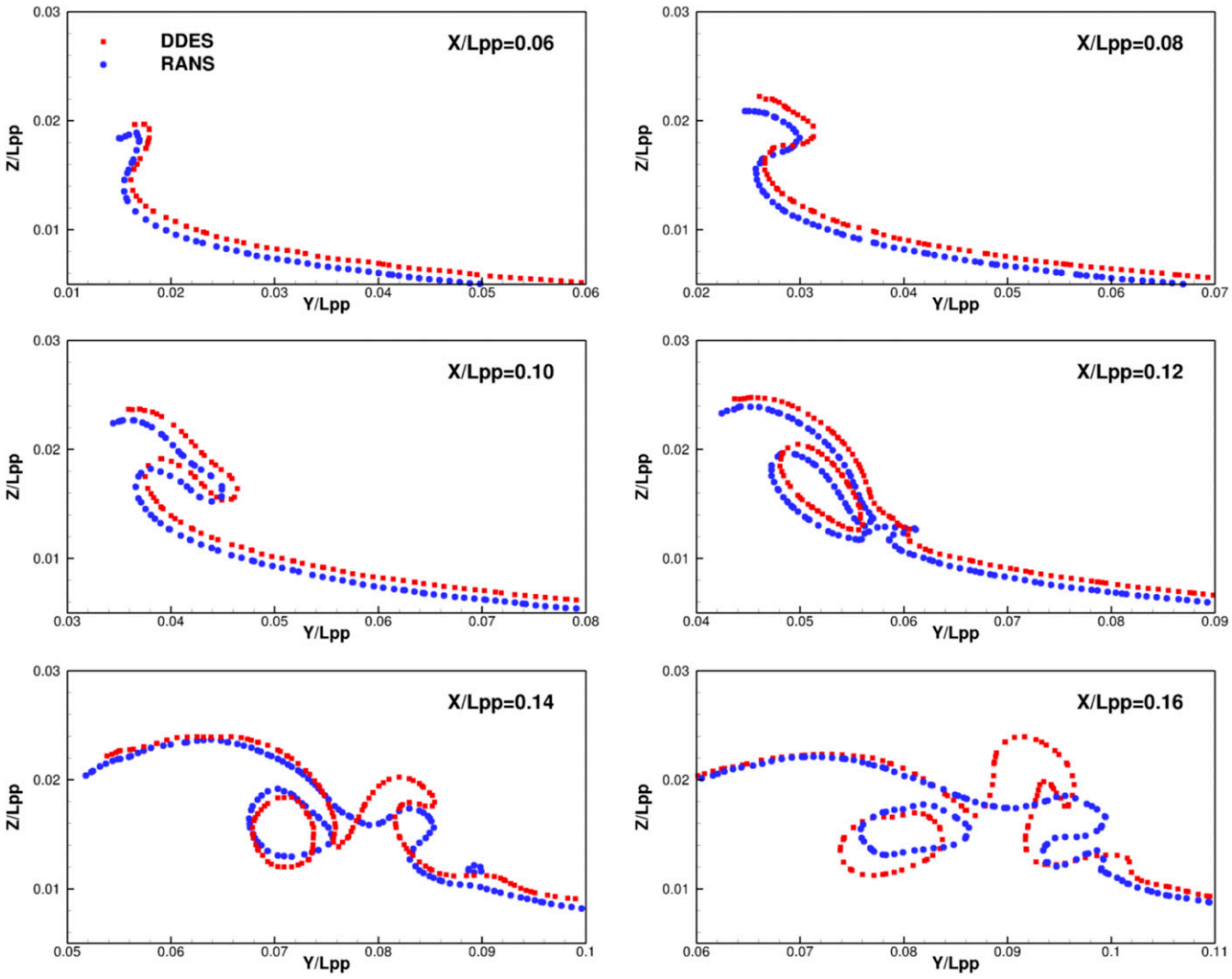

Fig. 9 Comparison of URANS and DDES results of breaking bow waves at Fn = .40

region of the overturning wave, negative axial vorticity was generated in the process when the initial plunger was falling. As soon as the tip of the initial plunger reconnects with the free surface, significant air entrainment happens, as shown in Fig. 10B.

A second plunger appears at section $x/L_{pp} = .15$, as shown in Fig. 10C. It can be seen that the axial vorticity distribution predicted by DDES is highly different from the URANS results, which is the main reason for the different shapes of breaking waves. According to the literature (Olivieri et al. 2007) considering breaking bow waves, scars can be observed in the bow wave region. In the present study, this phenomenon can also be noticed in Fig. 10C. The counter-rotating vortex pair represented as V1 and V2 is responsible for the scar, where the positive vorticity (V2) is generated and the second plunger is visible. When the tip of the initial plunger reconnects with the free surface, the interaction between the two parts causes the upward motion of the fluid and further leads to the positive vorticity and scar. The vortex pair has a rotating orientation and thus pumps fluid outboard, resulting in the second plunger. At $x/L_{pp} = .20$, there are two obvious air pockets in the DDES results, whereas the second plunger is not well resolved. In addition, the strength of the axial vorticity at the tip of the second plunger is smaller with the URANS result. At the far field with $x/L_{pp} = .25$, dissipation of the vorticity in URANS results is noticeable compared with the DDES results. Consequently, the free surface is smoother in the URANS computations.

The layouts of bow wave colored by axial vorticity in a series of planes are presented in Fig. 11. It is obvious that the bow wave at higher ship speed will cause an increase in vorticity at free surface. At Fn = .35, only two plungers occurred, where the influence of bow waves in the URANS simulation is less than that of DDES results. However, at Fn = .40, there were three plungers and all the three breakers were fully developed in the DDES.

It can be clearly seen that vorticity dissipates quickly in the present URANS computation, leading to the significant difference of the bow waves. The present work is just a preliminary study of the high-speed KCS ship bow waves; thus, not much validation work has been carried out. Nevertheless, it is convincible that the DDES approach is more appropriate for the simulation of high-speed ships, especially when breaking waves are considered.

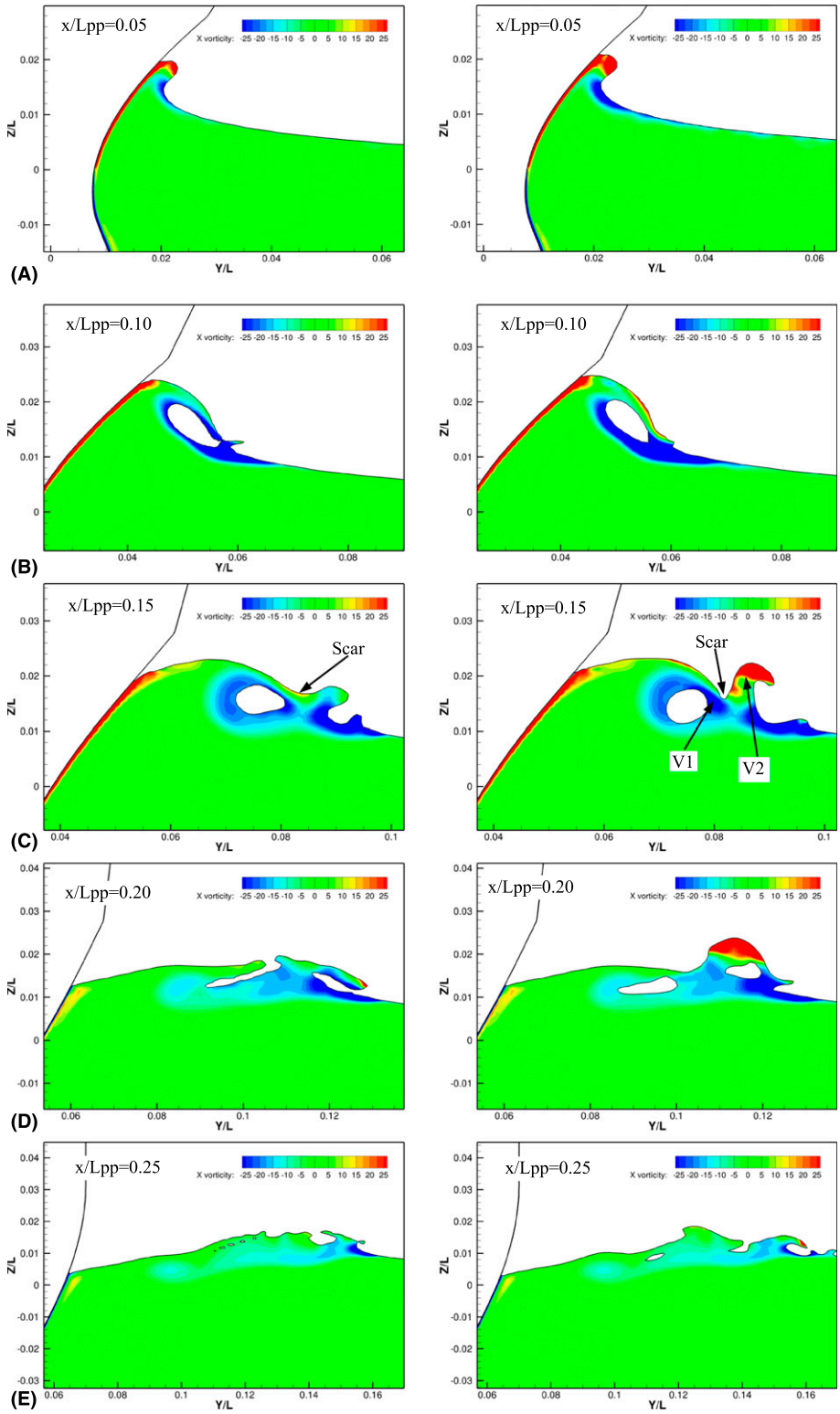

Fig. 10 Axial vorticity distribution (left column: URANS results, right column: DDES results)

5. Conclusions

In the present work, a preliminary study for a high-speed KCS ship model is performed to study the detailed flow around ship hull, especially for the breaking bow waves. The Fr = .26 case is conducted to verify the accuracy of the present numerical method. The predicted resistance and wave pattern are in good agreement with the experimental data using both URANS and DDES

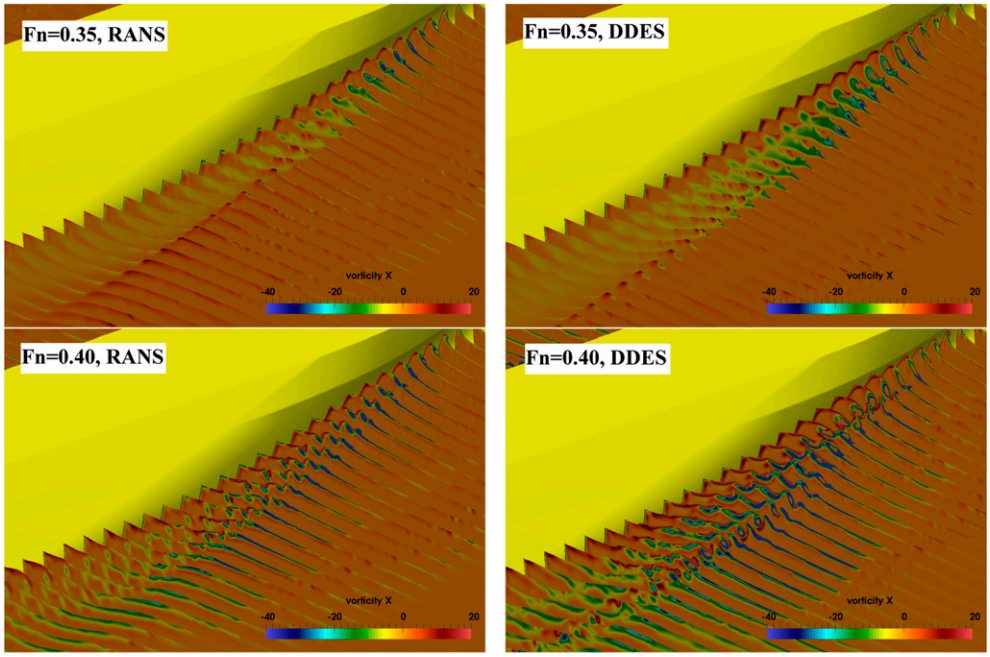

Fig. 11 Evolution of axial vorticity downstream

approaches. The predicted wave pattern of the high-speed case is compared with the experiment photos taken at the CSSRC. The wave-making phenomenon is more violent in the DDES results, which shows good agreement with the experiment photos. The predicted wave profile on the hull surface at the bow region and free surface cut shows an overall agreement with the available measurements. Detailed flow information, such as wave profiles on the hull surface and vorticity field around the free surface, is presented to illustrate the flow characters. It is shown that the variation of vorticity is mainly concentrated near the free surface. The vorticity dissipates quickly in the present URANS computation, leading to the significant difference of the bow waves compared with the DDES results. Although there are no available experimental flow data to validate the present computation results, it is still convincible that the DDES approach is more appropriate for the simulation of high-speed ships, especially when considering the breaking waves.

Future work will be focused on more validation work for the present numerical simulations, including the sensitivity study of related parameters. The present simulations can also provide valuable guidance for the towing tank measurements of breaking bow waves, especially for the measured regions and flow parameters.

Acknowledgments

This work is supported by the National Natural Science Foundation of China (51809169, 51879159, 51490675, 11432009, and 51579145), The National Key Research and Development Program of China (2019YFB1704204), Chang Jiang Scholars Program (T2014099), Shanghai Excellent Academic Leaders Program (17XD1402300), Program for Professor of Special Appointment (Eastern Scholar) at Shanghai Institutions of Higher Learning (2013022), Innovative Special Project of Numerical Tank of Ministry of Industry and Information Technology of China (September 23, 2016), and Lloyd's Register Foundation for doctoral student, to which the authors are most grateful.

References

Berberović, E., van Hinsberg, N., Jakirlić, S., Roisman, I., and Tropea, C. 2009 Drop impact onto a liquid layer of finite thickness: Dynamics of the cavity evolution, *Physical Review E*, **79**(3), 36306.

Broglia, R. and Durante, D. 2018 Accurate prediction of complex free surface flow around a high speed craft using a single-phase level set method, *Computational Mechanics*, **62**(3), 421–437.

Cao, H. and Wan, D. C. 2017 Benchmark computations of wave run-up on single cylinder and four cylinders by naoe-FOAM-SJTU solver, *Applied Ocean Research*, **65**, 327–337.

Carrica, P. M., Huang, J., Noack, R., Kaushik, D., Smith, B., and Stern, F. 2010 Large-scale DES computations of the forward speed diffraction and pitch and heave problems for a surface combatant, *Computers & Fluids*, **39**(7), 1095–1111.

Dong, R. R., Katz, J., and Huang, T. T. 1997 On the structure of bow waves on a ship model, *Journal of Fluid Mechanics*, **346**, 77–115.

Issa, R. I. 1986 Solution of the implicitly discretised fluid flow equations by operator-splitting, *Journal of Computational Physics*, **62**(1), 40–65.

Kornev, N., Shevchuk, I., Abbas, N., Anschau, P., and Samarbakhsh, S. 2019 Potential and limitations of scale resolved simulations for ship hydrodynamics applications, *Ship Technology Research*, **66**(2), 83–96.

Longo, J. and Stern, F. 2002 Effects of drift angle on model ship flow, *Experiments in Fluids*, **32**(5), 558–569.

Marrone, S., Bouscasse, B., Colagrossi, A., and Antuono, M. 2012 Study of ship wave breaking patterns using 3D parallel SPH simulations, *Computers & Fluids*, **69**, 54–66.

Marrone, S., Colagrossi, A., Antuono, M., Lugni, C., and Tulin, M. P. 2011 A 2D+t SPH model to study the breaking wave pattern generated by fast ships, *Journal of Fluids and Structures*, **27**(8), 1199–1215.

Menter, F. R. 1994 Two-equation eddy-viscosity turbulence models for engineering applications, *AIAA Journal*, **32**(8), 1598–1605.

Menter, F. R., Kuntz, M., and Langtry, R. 2003 Ten years of industrial experience with the SST turbulence model, *Turbulence, Heat and Mass Transfer*, **4**(1), 625–632.

Mousaviraad, S. M., Wang, Z., and Stern, F. 2015 URANS studies of hydrodynamic performance and slamming loads on high-speed planing hulls in calm water and waves for deep and shallow conditions, *Applied Ocean Research*, **51**, 222–240.

Olivieri, A., Pistani, F., Wilson, R., Campana, E. F., and Stern, F. 2007 Scars and vortices induced by ship bow and shoulder wave breaking, *Journal of Fluids Engineering*, **129**(11), 1445–1459.

Ren, Z., Wang, J., and Wan, D. C. 2018 Numerical study of the effects of grid scale on bow wave breaking, *Proceedings*, The Twenty-Eighth International Ocean and Polar Engineering Conference, June 10–15, Sapporo, Japan, 94–101.

Roth, G. I., Mascenik, D. T., and Katz, J. 1999 Measurements of the flow structure and turbulence within a ship bow wave, *Physics of Fluids*, **11**(11), 3512–3523.

Shen, Z., Wan, D. C., and Carrica, P. M. 2015 Dynamic overset grids in OpenFOAM with application to KCS self-propulsion and maneuvering, *Ocean Engineering*, **108**, 287–306.

Spalart, P. R., Deck, S., Shur, M. L., Squires, K. D., Strelets, M. K., and Travin, A. 2006 A new version of detached-eddy simulation, resistant to ambiguous grid densities, *Theoretical and Computational Fluid Dynamics*, **20**(3), 181–195.

Spalart, P. R. 2009 Detached-eddy simulation, *Annual Review of Fluid Mechanics*, **41**(1), 181–202.

Wang, J. and Wan, D. C. 2017 Breaking wave simulations of high-speed surface combatant using OpenFOAM, *Proceedings*, The 8th International Conference on Computational Methods (ICCM 2017), July 25–29, Guilin, China.

Wang, J., Zou, L., and Wan, D. C. 2017 CFD simulations of free running ship under course keeping control, *Ocean Engineering*, **141**, 450–464.

Wang, J., Zou, L., and Wan, D. C. 2018 Numerical simulations of zigzag maneuver of free running ship in waves by RANS-Overset grid method, *Ocean Engineering*, **162**, 55–79.

Wang, J., Zhao, W., and Wan, D. C. 2019 Development of naoe-FOAM-SJTU solver based on OpenFOAM for marine hydrodynamics, *Journal of Hydrodynamics*, **31**(1), 1–20.

Wilson, R. V., Carrica, P. M., and Stern, F. 2006 URANS simulations for a high-speed transom stern ship with breaking waves, *International Journal of Computational Fluid Dynamics*, **20**(2), 105–125.

Ye, H. and Wan, D. C. 2017 Benchmark computations for flows around a stationary cylinder with high Reynolds numbers by RANS-overset grid approach, *Applied Ocean Research*, **65**, 315–326.

Zhao, W. and Wan, D. C. 2016a Detached-eddy simulation of flow past tandem cylinders, *Applied Mathematics and Mechanics*, **37**(12), 1272–1281.

Zhao, W. and Wan, D. C. 2016b Numerical study of 3D flow past a circular cylinder at subcritical reynolds number using SST-DES and SST-URANS, *Chinese Journal of Hydrodynamics*, **31**(1), 1–8.

Zhao W., Zou L., and Wan D. C. 2018 Numerical investigation of vortex-induced motions of a paired-column semisubmersible in currents, *Ocean Engineering*, **164**, 272–283.